

# In-situ remediation of deep petroleum-contaminated soil injection

Wang Yajun<sup>1,2</sup> Dong Wantao<sup>1</sup> Chen Tianjing<sup>1</sup> Li Li<sup>3</sup>

Zhang Yurong<sup>1</sup> Xu Shenghui<sup>1</sup> Fu Dafang<sup>1,2</sup>

(<sup>1</sup>School of Civil Engineering, Lanzhou University of Technology, Lanzhou 730000, China)

(<sup>2</sup>SEU-Monash Joint Research Center for Future Cities, Suzhou 215123, China)

(<sup>3</sup>China Railway Research Institute Co., Ltd. Chengdu Branch, Chengdu 610000, China)

**Abstract:** A computational fluid dynamics (CFD) numerical simulation and field experiment were used to investigate optimal operating parameters of high-pressure jet grouting equipment and clarify the boundary law of the injection area in the remediation process. The response surface optimization design results show that the optimal injection pressure is 30 MPa, rotation speed is 23 r/min, commission speed is 30 cm/min, and the optimal injection diameter is 147.3 cm. Based on the CFD numerical simulation, the ratio of the injection core, turbulent zone, and seepage zone is approximately 1:4:2. The distribution law of jet core, turbulence zone and seepage zone at different cross-sections under 30 MPa operating conditions is as follows: The jet core radius is approximately 100 mm, the turbulence zone is mainly distributed at 100 to 500 mm, the seepage zone is mainly distributed at 500 to 700 mm, the seepage zone could be completed within 2 h, and the proportion of the three boundary zones in the injection zone is similar to that of the numerical simulation. This study provides theoretical parameters and practical reference for the remediation of deep pollution via in-situ chemical oxidation in the Loess Plateau soil environment.

**Key words:** in-situ chemical oxidation; high-pressure jet; total petroleum hydrocarbons; remediation of contaminated soil; computational fluid dynamics (CFD) numerical simulation

**DOI:** 10.3969/j.issn.1003-7985.2021.04.008

The extensive exploitation, transportation, and processing of early oil caused a large number of land pollution, water environment pollution and air pollution problems, and it was difficult to solve for a long time. The task of environmental protection and pollution control has become more arduous.

**Received** 2021-04-19, **Revised** 2021-08-20.

**Biography:** Wang Yajun (1979—), male, doctor, associate professor, wyj79626@163.com.

**Foundation items:** The National Natural Science Foundation of China (No.41967043, 52160003), the Natural Science Foundation of Gansu Province (No.20JR5RA461), the Key Project of China Railway Southwest Research Institute Co., Ltd. (No.2018-KJ003-Z003-XB), the Industrial Support Program of the Higher Education of Gansu Province (No.2020C-40).

**Citation:** Wang Yajun, Dong Wantao, Chen Tianjing, et al. In-situ remediation of deep petroleum-contaminated soil injection[J]. Journal of Southeast University (English Edition), 2021, 37(4): 394 – 400. DOI: 10.3969/j.issn.1003-7985.2021.04.008.

Soil remediation technologies can be divided into three categories: physical method<sup>[1]</sup>, chemical method<sup>[2]</sup>, and biological method<sup>[3]</sup>. Chemical remediation has been widely used in recent years. This method can greatly shorten the remediation cycle and has a strong ability to remove petroleum pollutants to reduce the cost of secondary land use<sup>[4-6]</sup>. Wu et al.<sup>[7]</sup> used chemical oxidation technology to repair petroleum-contaminated soil, and the removal rate could reach 82.1% in 7 d. Ouriache et al.<sup>[8]</sup> used chemical oxidation technology to repair petroleum contaminated soil with a total petroleum hydrocarbons (TPH) removal rate of 72.2% in 2 d. Repair methods include in situ repair and ectopic repair. In situ chemical oxidation technology has been widely used due to its fast repair speed and high universality<sup>[9]</sup>. High-pressure rotary jet technology is often used in the remediation of deep soil pollution due to the advantages of precise injection and efficient mixing<sup>[10]</sup>.

First, the response surface optimization design was used to determine the optimal operating conditions and parameters of high-pressure jet grouting equipment. Then, the formation rules of the boundary layer in the jet environment were simulated. Finally, field injection experiments were performed, and their results were compared with the numerical simulation results.

## 1 Experiment

### 1.1 Soil physical and chemical properties and pollution distribution in the experimental site

The research object of this experiment is the soil sample collected from the eastern part of Gansu Province, where Huangmian soil is mainly distributed. Huangmian soil is an erosive soil formed by the continuous development of Malan or Lishi loess parent material exposed to the erosion of various development layers of black loessial soil. It is characterized by loose structure, developed vertical joints, rock hard when dry, weak resistance to water, easy erosion, and poor water retention performance<sup>[11-12]</sup>. Based on the field sampling analysis, the physical and chemical properties of the soil in the pilot test site are shown in Tab.1.

**Tab. 1** The physical and chemical properties of Huangmian soil

| Organic matter content/<br>(g · kg <sup>-1</sup> ) | Total petroleum hydrocarbons content/<br>(mg · kg <sup>-1</sup> ) | Mechanical composition/% |                 |               |               |
|--|---|--------------------------|-----------------|---------------|---------------|
|  |   | Sand particle            | Powder particle | Clay particle | Physical clay |
| 56.34  | 7 199.99  | 21.35                    | 68.92           | 9.73          | 22.68         |

## 1.2 Process flow of the field device

The main equipment of a high-pressure rotary jet drilling rig includes a drill pipe, drill bit, drilling rig, gyra-tor, lifter, automatic rotary table, high-pressure pump, high-pressure pipeline, radiator, and console. The jet region can be divided into the jet core area, turbulent region, and seepage region. The jet core area is mainly composed of high-pressure fluid. After injection, a round hole will be left due to the strong cutting force of the water flow. The high-pressure rotary jet technology is shown in Fig. 1.

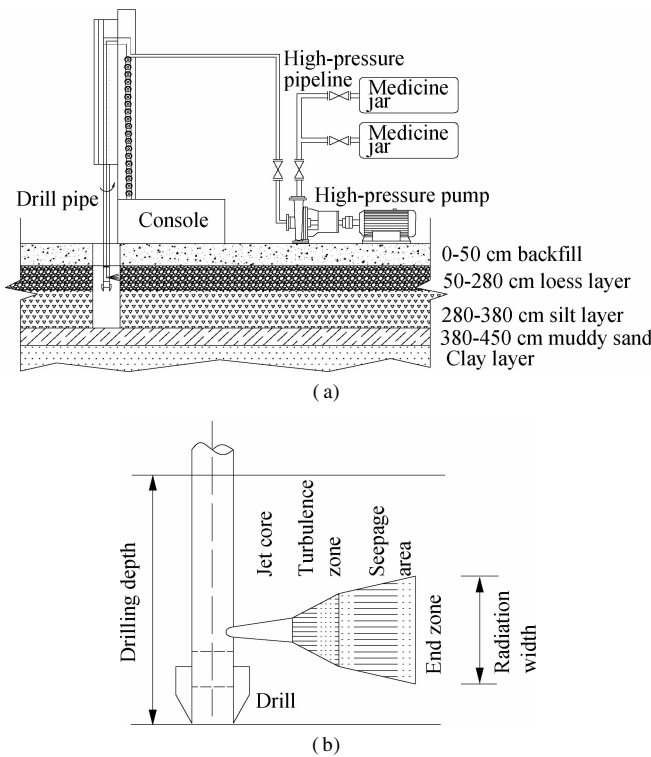


**Fig. 1** Process diagram of the high-pressure rotary jet technology. (a) Process diagram; (b) Schematic diagram of the injection area rotary spray equipment

## 1.3 Instruments and reagents

Instruments include infrared spectrophotometer (OIL-460, Beijing Huaxia Science and Technology Co., Ltd.), multi-purpose cyclotron oscillator (HY-5, Jiangsu Zhengji Instrument Co., Ltd.), and ultraviolet-visible spectrophotometer (UV-1780, Shimadzu Instrument Co., Ltd.).

Reagents include hydrogen peroxide (H<sub>2</sub>O<sub>2</sub>, 30%), anhydrous sodium sulfate (Na<sub>2</sub>SO<sub>4</sub>, 99%), ferrous sul-

fate heptahydrate (FeSO<sub>4</sub> · 7H<sub>2</sub>O, 99%), sodium bicarbonate (NaHCO<sub>3</sub>, 99.5%), sodium ferrate (Na<sub>2</sub>FeO<sub>4</sub>, 99%), and carbon tetrachloride (CCl<sub>4</sub>, 99.5%).

## 1.4 Experimental methods

The parameters to be determined were injection pressure, drill pipe rotation speed, lifting speed, and injection diameter. The injection volume was recorded on site, and the injection diameter was measured by an excavator. Design-Expert 10.0.7 was used to design the experiment; the Box-Behnken experimental design was utilized as the design principle; the injection pressure, drill pipe rotation speed, and lifting speed were taken as the investigation factors; and the injection diameter (*y*) was used as the response value. The Box-Behnken experimental design, which has a total of 17 groups of experiments, is shown in Tab. 2.

**Tab. 2** Box-Behnken experimental design

| Level | Injection pressure/MPa | Drill pipe rotation speed/(r · min <sup>-1</sup> ) | Lifting speed/(cm · min <sup>-1</sup> ) |
|-------|------------------------|--|---|
| -1    | 10                     | 15   | 10                                      |
| 0     | 20                     | 20   | 25                                      |
| 1     | 30                     | 25   | 40                                      |

The remediation experiment of the contaminated site was conducted in zone 2. In order to leave no blank, the plum-blossom distribution method was adopted, as shown in Fig. 1(b).

The model of the porous media aims to add a momentum source term into the standard fluid flow equation,

$$S_i = - \left( \sum_{j=1}^3 D_{ij} \mu \nu_j + \sum_{j=1}^3 C_{ij} \frac{1}{2} \rho |\nu| \nu_j \right) \quad (1)$$

where  $S_i$  is the source term of  $i(x, y, z)$  momentum equation;  $\nu$  is the velocity vector, m/s;  $\rho$  is the density, kg/m<sup>3</sup>;  $\mu$  is the dynamic viscosity coefficient, Pa · s; and  $D$  and  $C$  are the matrices.

The momentum source term consists of two parts: viscous loss term and inertial loss term. The first term on the right side of Eq. (1) is the viscous loss term, and the second term is the inertial loss term.

In porous media, the pressure drop is usually proportional to the velocity.

$$\nabla p = - \frac{\mu}{\alpha} \nu \quad (2)$$

Without considering the convection acceleration and diffusion, the porous medium model could be reduced to Darcy's law (Eq. (2)).

$$\nabla p_x = \sum_{j=1}^3 \frac{\mu}{\alpha_{xj}} \nu_j \Delta n_x \quad (3)$$

$$\nabla p_y = \sum_{j=1}^3 \frac{\mu}{\alpha_{yj}} \nu_j \Delta n_y \quad (4)$$

$$\nabla p_z = \sum_{j=1}^3 \frac{\mu}{\alpha_{zj}} \nu_j \Delta n_z \quad (5)$$

where  $\nabla p$  is the pressure drop, and  $1/\alpha$  is the viscous resistance coefficient,  $\text{m}^{-2}$ . The pressure drop in  $X$ ,  $Y$ , and  $Z$  directions is calculated by Eqs. (3), (4) and (5), respectively.

$\Delta n_x$ ,  $\Delta n_y$ , and  $\Delta n_z$  are the thickness of porous media. If the thickness used in the model is different from the actual thickness, then it must be adjusted. The spatial structure of this area was constructed by  $500\text{ mm} \times 2\,000\text{ mm}$  soil particles with the same particle size. The calculation grid file of the two-dimensional model was generated by Gambit. The relevant parameters of the model simulation are shown in Tab. 3.

Tab.3 Model simulation parameters

| Injection pressure/MPa | Porosity/% | Soil density/( $\text{kg} \cdot \text{m}^{-3}$ ) | Viscosity/( $\text{Pa} \cdot \text{s}$ ) | Calculation domain (length $\times$ width)/(mm $\times$ mm) |
|------------------------|------------|--|--|---|
| 30                     | 57.15      | 1 852  | 300                                      | 2 000 $\times$ 500  |

### 1.5 Analysis method

The determination of the molar concentration of  $\text{Na}_2\text{FeO}_4$  was performed as follows: determine the molar concentration of  $\text{Na}_2\text{FeO}_4$  via ultraviolet spectrophotometry, measure 41 mL of  $\text{Na}_2\text{FeO}_4$ , make a constant volume of a saturated sodium hydroxide solution to 10 mL, transfer the solution to a centrifuge tube, centrifuge at 3 000 r/min for 10 min, and measure the absorbance at a wavelength of 505 nm. The measured solution concentration multiplied by the dilution multiple was the molar concentration of the sample solution<sup>[13]</sup>. Petroleum pollutants in soil were determined via infrared spectrophotometry (HJ 1051—2019).

## 2 Results and Discussion

### 2.1 Response surface methodology for the optimization of the influencing factors of high-pressure jet grouting

Brilliant blue FCF was used as the tracer in the experiment. According to the Box-Behnken design principle and the actual working conditions of the high-pressure rotary jet equipment, three important factors need to be considered: injection pressure (20 MPa), commission speed (25 cm/min), and rotation speed (20 r/min). These factors were taken as the central points to perform the response surface analysis. The injection pressure ( $A$ ), rotation speed ( $B$ ), and commission speed ( $C$ ) were taken as independent variables and the injection diameter ( $Y$ ) as the response value to design a three-factor and three-level experiment. Design-Expert 10.0.7 was used to analyze the model, investigate the relationship among the factors, and predict the best repair process. The variance analysis results are shown in Tab. 4. The injection

diameter represents the diameter of the circle formed after the entire spinning process is over.

$$Y = 109.8 + 25.63A + 6.38B + 3.5C + 5AB - 1.25AC + 2.25BC + 4.85A^2 - 2.15B^2 - 3.4C^2 \tag{6}$$

Tab.4 Analysis of the variance of the regression equation

| Source          | SS       | DOF | MSE      | F      | P        |
|-----------------|----------|-----|----------|--------|----------|
| Model           | 5 961.69 | 9   | 662.41   | 79.19  | <0.000 1 |
| A               | 5 253.13 | 1   | 5 253.13 | 628.04 | <0.000 1 |
| B               | 325.13   | 1   | 325.13   | 38.87  | 0.000 4  |
| C               | 98.00    | 1   | 98.00    | 11.72  | 0.011 1  |
| AB              | 100.00   | 1   | 100.00   | 11.96  | 0.010 6  |
| AC              | 6.25     | 1   | 6.25     | 0.75   | 0.416 0  |
| BC              | 20.25    | 1   | 20.25    | 2.42   | 0.163 7  |
| A <sup>2</sup>  | 99.04    | 1   | 99.04    | 11.84  | 0.010 8  |
| B <sup>2</sup>  | 19.46    | 1   | 19.46    | 2.33   | 0.171 0  |
| C <sup>2</sup>  | 48.67    | 1   | 48.67    | 5.82   | 0.046 6  |
| Residual        | 58.55    | 7   | 8.36     |        |          |
| Misfit term     | 13.75    | 3   | 4.58     | 0.41   | 0.755 6  |
| Pure error      | 44.80    | 4   | 11.20    |        |          |
| Total deviation | 6 020.24 | 16  |          |        |          |

The quadratic multiple regression(Eq. (6)) of the coded variable was obtained through the regression fitting of each factor.

The model term  $F$  is equal to 79.19;  $P < 0.000\,1$ . The determination coefficient  $R^2$  was 99.03%, and the corrected determination coefficient  $R^2_{\text{adj}}$  was 97.78%. The misfit term  $P = 0.755\,6 > 0.05$  was not significant. Therefore, the fitting regression equation could be used to predict the radiation range of a high-pressure rotary sprayer in soil. Design-Expert 10.0.7 was used to analyze the regression equation. The distribution of the predicted and experimental values is shown in Fig. 2, and the contour and response surface are shown in Fig. 3.

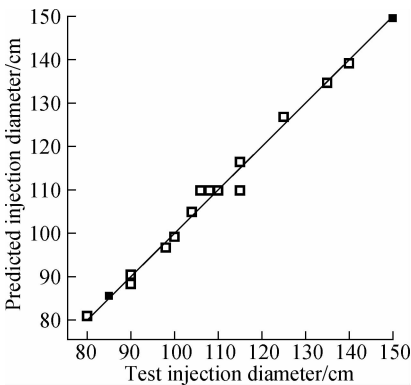
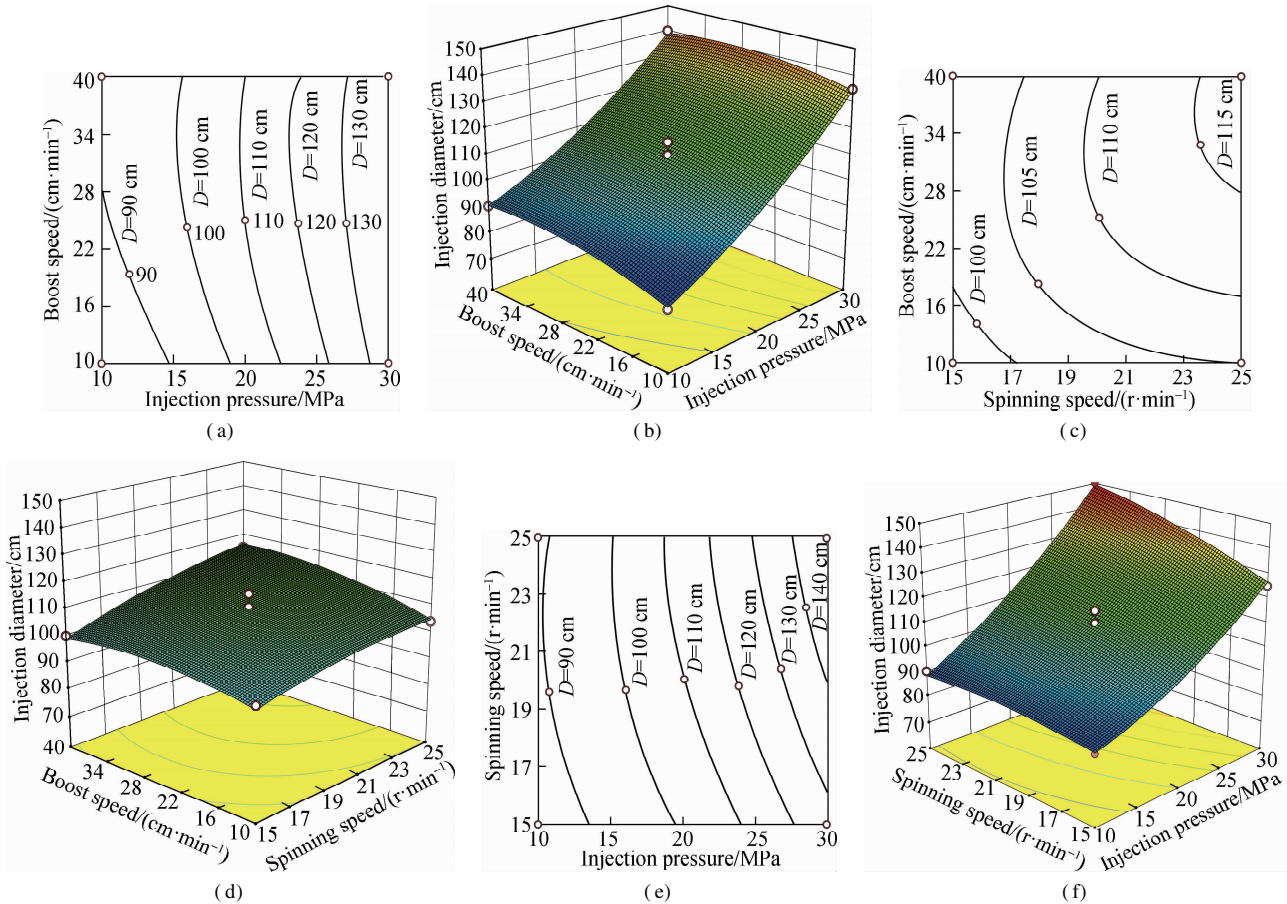


Fig.2 Distribution diagram of the test and predicted values of the injection diameter

Fig. 3 shows that the difference between the predicted value and experimental value is small, and the model could be used for experimental guidance. The contour and response surface of the injection diameter( $D$ ) with the three factors are shown in Fig. 4. Based on the  $P$  val-



**Fig. 3** Contour lines and response surface plots of the influence of the interaction of the three factors on the injection diameter. (a) AC 2D; (b) AC 3D; (c) BC 2D; (d) BC 3D; (e) AB 2D; (f) AB 3D

ue of each parameter in Tab. 5, the primary terms  $A$ ,  $B$ , and  $C$ , interaction terms  $AB$ , secondary terms  $A^2$  and  $C^2$ , and the  $P$  value were less than 0.05. This finding indicated that they had a significant impact on the response value  $Y$ . The interaction terms  $AC$  and  $BC$ , quadratic terms  $B^2$ , and  $P$  values were greater than 0.05. This finding indicated that the impact on the response value  $Y$  was not significant.

Based on the quadratic regression equation, the optimal operating conditions of the high-pressure rotary sprayer are as follows: Injection pressure is 30 MPa, rotation speed is 23 r/min, commission speed is 30 cm/min, and injection diameter is 147.3 cm. Three validation experiments were performed under the optimized conditions, and the actual value is 144 cm, which is close to the predicted value. The results show that the quadratic regression equation could accurately predict the influence of the three factors on the injection diameter, and the response surface optimization design showed that the scheme with the largest injection diameter under the optimal working condition was reliable.

2.2 The boundary layer of the solute transport

Based on the above experimental conclusions, 30 MPa

injection pressure was used for the simulation, and the injection pressure was set with the pressure around 5 m deep soil. Here, the soil density was 1 852 kg/m<sup>3</sup>, the porosity was 57.15%, and the viscosity was 300 Pa · s. The nozzle was set at 100 mm inside the grid, and the spray area was a 0.5 m × 2 m two-dimensional rectangular grid. Fluent software was used for the simulation calculation.

As shown in Figs. 4 and 5, the distribution was symmetrical in the longitudinal direction, and radial jet in the transverse direction. The jet velocity was 243 m/s at the nozzle position and attenuated to 55.7 m/s at 100 mm, and the velocity decreased by 77.1%. This area mainly existed in the form of mud. The mud near the jet core had strong fluidity, and the farther away from the jet core, the lesser the fluidity. A seepage area was formed between 500 and 700 mm. At this time, the jet velocity

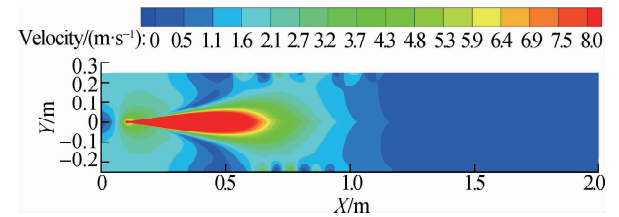


**Fig. 4** Jet velocity distribution diagram

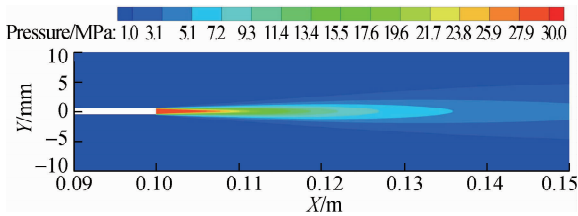


Fig. 5 Jet flow pressure distribution diagram

and jet pressure were reduced by 98.7% and 99.8%, respectively. The formation of this area could be completed within 2 h.

Six sections in the jet direction were selected to observe the changes in the dynamic pressure and turbulent kinetic

energy. Figs. 6 and 7 show that the spray diameter at 50 mm from the nozzle was 20 mm, the dynamic pressure at the center point to the edge position quickly decays, the dynamic pressure was mainly concentrated at the center point, and the diffusion movement was weak. The turbulent kinetic energy distribution at 50 mm away from the nozzle showed that the turbulent kinetic energy around the jet center point was larger, and the turbulent kinetic energy attenuated to 0 at 15 mm away from the jet boundary. As the position of the nozzle becomes increasingly farther, the position where the turbulent kinetic energy acts is also farther away.

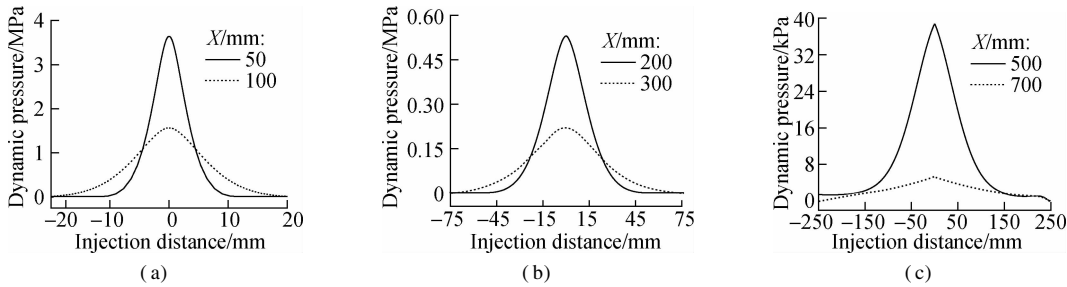


Fig. 6 Dynamic pressure distribution diagram of the flow direction position profile. (a)  $X=50, 100$  mm; (b)  $X=200, 300$  mm; (c)  $X=500, 700$  mm

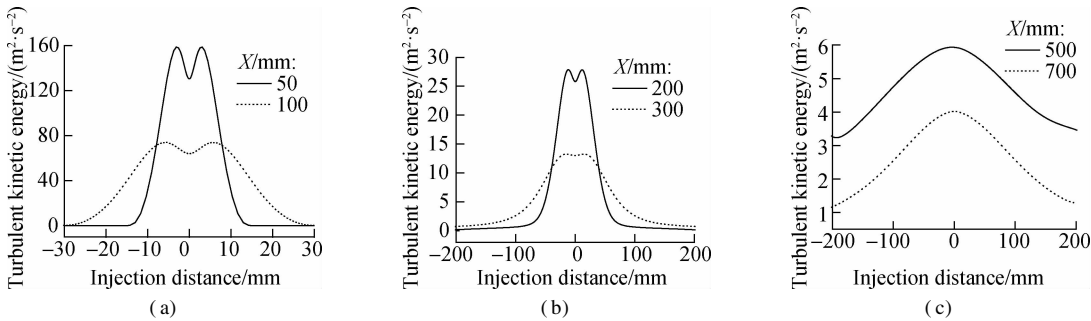


Fig. 7 Turbulent kinetic energy distribution diagram of the flow direction position profile. (a)  $X=50, 100$  mm; (b)  $X=200, 300$  mm; (c)  $X=500, 700$  mm

Five cross-sections were selected at the radial position of the jet to observe the changes in the dynamic pressure and turbulent kinetic energy. As shown in Fig. 8, at the position of the jet centerline, when the distance from the nozzle was 300 mm, the dynamic pressure change began to slow down, but the section dynamic pressure began to increase at 100 mm from the centerline. This finding showed that when the distance from the nozzle was 300

mm, the dynamic pressure mainly acted on the centerline position. As shown in Fig. 9, the turbulent kinetic energy around the centerline was larger in this range, and the hydraulic cutting effect was evident. This condition was consistent with the field experiment. In this range, the closer the mud to the nozzle position, the easier it was to return the slurry.

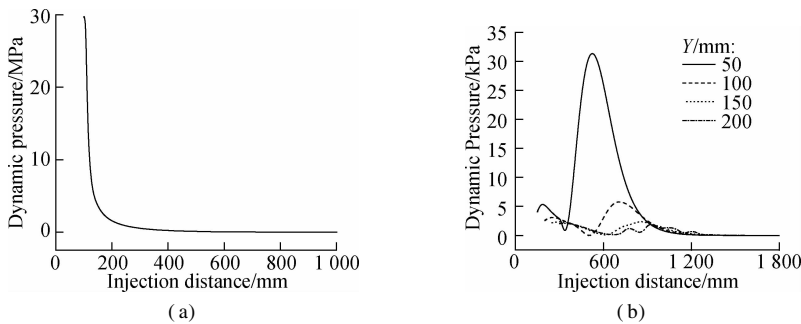


Fig. 8 Radial position section dynamic pressure distribution diagram. (a)  $Y=0$ ; (b)  $Y=50, 100, 150, 200$  mm

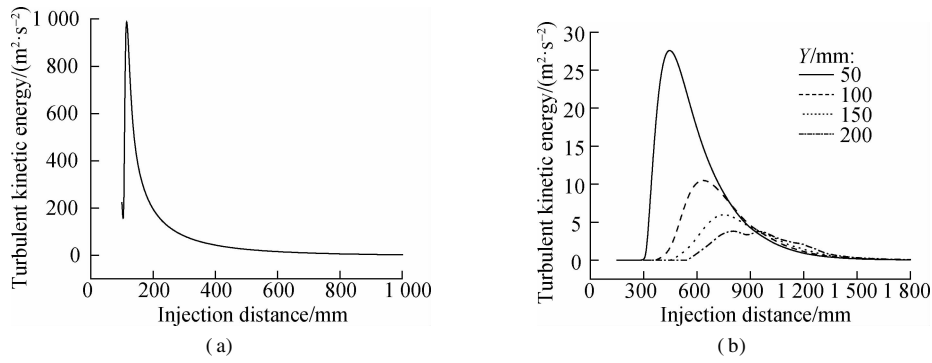


Fig. 9 Radial position profile turbulent kinetic energy distribution diagram. (a)  $Y=0$ ; (b)  $Y=50, 100, 150, 200$  mm

### 2.3 Comparative study of the field experiment and simulation experiment

The average total petroleum hydrocarbon content of the restoration site was 7 199.99 mg/kg soil. The repairing agents were  $\text{Na}_2\text{FeO}_4$ ,  $\text{KIO}_4$ ,  $\text{NaHCO}_3$ , and  $\text{Na}_2\text{S}_2\text{O}_8$ .  $\text{KIO}_4$  and  $\text{NaHCO}_3$  were  $\text{Na}_2\text{FeO}_4$  stabilizers. The mass percentage concentrations of  $\text{KIO}_4$  and  $\text{NaHCO}_3$  were 0.1% and 0.15%, respectively, and  $\text{Na}_2\text{S}_2\text{O}_8$  was the  $\text{Na}_2\text{FeO}_4$  activator. The amount of  $\text{Na}_2\text{S}_2\text{O}_8$  was 2 g/kg soil. The amount of  $\text{Na}_2\text{FeO}_4$  was 7.5 g/kg soil. The repairing step was to inject the  $\text{Na}_2\text{S}_2\text{O}_8$  solution after 4 h of injection of the mixed solution of  $\text{Na}_2\text{FeO}_4$ ,  $\text{KIO}_4$ , and  $\text{NaHCO}_3$ . Based on the comparison of the field experiment and simulation experiment results, the ratio of the jet core, turbulence zone, and seepage zone is approximately 1:4:2. The field experiment and simulation experiment had a good fit, and the simulation could provide a certain theoretical basis for the actual project (see Tab.5).

Tab.5 Comparison of the field experiment and simulation experiment results

| Injection area | Jet core radius/mm | Turbulence zone/mm | Seepage zone/mm |
|----------------|--------------------|--------------------|-----------------|
| Field          | 90 to 110          | 410 to 450         | 180 to 230      |
| Simulation     | 100                | 400                | 200             |
| Removal rate/% | 87.1               | 82.5               | 76.3            |

The repair effect was reduced to the lowest 11 d after the injection of the agent. The highest removal rate was 87.1%, concentrated near the jet core, and the lowest removal rate was 76.3%, concentrated near the seepage area. The plum-blossom dots can solve the problem of reduced total petroleum hydrocarbons removal rate in the seepage area. The TPH removal rate in the seepage zone can be stabilized at 83.77%.

### 3 Conclusions

1) The best operating conditions of the high-pressure rotary injection machine are as follows: Injection pressure is 30 MPa, rotation speed is 23 r/min, and commission speed is 30 cm/min. The best injection diameter is 147.3 cm.

2) The core radius is approximately 100 mm, the turbulence zone is mainly distributed at 100 to 500 mm, the seepage zone is mainly distributed at 500 to 700 mm, and the seepage area could be completed within 2 h.

3) Based on the numerical simulation, the effective radiation radius under the injection pressure of 30 MPa is 800 mm, and the effective radius of the jet direction section is 200 mm. The simulation results are similar to the experimental results. The comparison of the field experiment and simulation experiment results could confirm that the ratio of the jet core, turbulent flow zone, and seepage zone is approximately 1:4:2.

### References

- [1] Chen Y, Zhao R Z, Xue J, et al. Generation and distribution of PAHs in the process of medical waste incineration [J]. *Waste Management*, 2013, **33**(5): 1165 – 1173. DOI: 10.1016/j.wasman.2013.01.011.
- [2] Ouriache H, Arrar J, Namane A, et al. Treatment of petroleum hydrocarbons contaminated soil by Fenton like oxidation[J]. *Chemosphere*, 2019, **232**: 377 – 386. DOI: 10.1016/j.chemosphere.2019.05.060.
- [3] Rittmann B E, McCarty P L. *Environmental biotechnology: Principles and application*[M]. Translated by Wen X H, Wang J L. Beijing: Tsinghua University Press, 2012.
- [4] Li L, Dong W T, Zhang X, et al. Research progress on remediation of oil-contaminated soil[J]. *Sichuan Environment*, 2020, **39**(4): 200 – 205. DOI: 10.14034/j.cnki.schj.2020.04.032. (in Chinese)
- [5] Zhang Z T, Chen Y, Chen D, et al. Review on bioremediation for the petroleum contaminated soil[J]. *Chinese Journal of Soil Science*, 2019, **50**(1): 246 – 252. DOI: 10.19336/j.cnki.trtb.2019.01.37. (in Chinese)
- [6] Zhang L, Wang Y L, Zhou P, et al. Co-bioremediation of petroleum-contaminated salt marsh by addition of petroleum-degrading bacteria and halophytes agent[J]. *Periodical of Ocean University of China*, 2018, **48**(S1): 57 – 63. DOI: 10.16441/j.cnki.hdxh.20160181. (in Chinese)
- [7] Wu H, Sun L N, Wang H, et al. Remediation of petroleum hydrocarbon-contaminated soils by  $\text{CaO}_2/\text{Fe}^{2+}$  activated persulfate[J]. *Environmental Chemistry*, 2016, **35**(4): 623 – 628. DOI: 10.7524/j.issn.0254-6108.2016.04.2015110101. (in Chinese)
- [8] Ouriache H, Arrar J, Namane A, et al. Treatment of petroleum hydrocarbons contaminated soil by Fenton like ox-

idation[J]. *Chemosphere*, 2019, **232**: 377 – 386. DOI: 10.1016/j.chemosphere.2019.05.060.

[9] Liu X W, Li R F, Li X, et al. A model of in situ remediation of TCE-contaminated soil by sodium persulfate [J]. *Acta Scientiae Circumstantiae*, 2013, **33**(11): 2935 – 2940. DOI: 10.13671/j.hjkxxb.2013.11.013. (in Chinese)

[10] Hidalgo P, Navia R, Hunter R, et al. Synthesis of carbon nanotubes using biochar as precursor material under microwave irradiation [J]. *Journal of Environmental Management*, 2019, **244**: 83 – 91. DOI: 10.1016/j.jenvman.2019.03.082.

[11] Jia H Y. The content movement and distribution characteristics of main soil types nutrient elements in hilly loess plateau [J]. *Research of Soil and Water Conservation*, 1998, **5**(1): 119 – 125. (in Chinese)

[12] Saritha A, Raju B, Narayana Rao D, et al. Facile green synthesis of iron oxide nanoparticles via solid-state thermolysis of a chiral, 3D anhydrous potassium tris(oxalato)ferrate(III) precursor [J]. *Advanced Powder Technology*, 2015, **26**(2): 349 – 354. DOI: 10.1016/j.appt.2014.11.005.

[13] Jia H D, Yang X L, Yang Y, et al. Direct spectro photometric determination of ferrate [J]. *Chinese Journal of Analytical Chemistry*, 1999, **27**(5): 617. DOI: 10.3321/j.issn:0253-3820.1999.05.031. (in Chinese)

## 深层石油类污染土壤注射原位修复

王亚军<sup>1,2</sup> 董万涛<sup>1</sup> 陈甜婧<sup>1</sup> 李 丽<sup>3</sup> 张玉蓉<sup>1</sup> 许生辉<sup>1</sup> 傅大放<sup>1,2</sup>

(<sup>1</sup> 兰州理工大学土木工程学院, 兰州 730000)  
(<sup>2</sup> 东南大学-莫纳什大学未来城市研究院, 苏州 215123)  
(<sup>3</sup> 中铁科学研究院有限公司成都分公司, 成都 610000)

**摘要:**采用 CFD 数值模拟和现场实验方法,考察高压旋喷设备最佳运行工况参数,探讨修复过程中注射区域分界规律.通过响应面优化设计得出高压旋喷运行最佳注射压力为 30 MPa,旋转速度为 23 r/min,提升速度为 30 cm/min,最佳注射直径为 147.3 cm.通过 CFD 数值模拟出注射区域分界的喷射核、湍流区和渗流区比例约为 1:4:2.在 30 MPa 运行工况下不同断面喷射核、湍流区和渗流区的分布规律为:喷射核半径在 100 mm 左右,湍流区主要分布在 100~500 mm 处,渗流区主要分布在 500~700 mm,且渗流区域可在 2 h 内完成.通过现场实验得到的注射区域 3 个分界区比例与数值模拟结果类似.该研究为黄土高原土壤环境下原位化学氧化修复深层污染提供了理论参数和实践参考.

**关键词:**原位化学氧化;高压旋喷;总石油烃;污染土壤修复;CFD 数值模拟

**中图分类号:**X53